Electronic Supplementary Information:

Cobalt Substitution Slows Forsterite Carbonation in Low-Water Supercritical Carbon Dioxide

John S. Loring*[a], Tenley E. Webb [a], Mark E. Bowden [a], Mark H. Engelhard [b], and Sebastien N. Kerisit *

[a] *Physical and Computational Sciences Directorate, Pacific Northwest National Laboratory, Richland, WA 99354, United States.*

[b] *Energy and Environment Directorate, Pacific Northwest National Laboratory, Richland, WA 99354, United States.*

*Corresponding Authors: john.loring@pnnl.gov and sebastien.kerisit@pnnl.gov

This file contains 11 Pages, 2 Tables, and 6 Figures.

In situ High-Pressure Infrared Spectroscopic Titrations. In situ high-pressure IR titrations with water were carried out in supercritical CO_2 ($scCO_2$) or $scCO_2$ + 1% H_2 at 50 °C and 90 bar using an automated fluid-delivery apparatus coupled to a custom-built high-pressure IR reaction cell with both transmission and attenuated total reflection (ATR) IR optics.[1, 2] IR spectra were collected using a Bruker Vertex 80V spectrometer equipped with a water-cooled source and a deuterated tri-glycine sulfate (DTGS) detector. The spectrometer was housed in an environmental chamber thermostated to 25 ± 0.2 °C. The high-pressure optical cell had an internal volume of 57.5 mL and was jacketed for temperature control by a circulating water bath. Temperature was monitored by a high-pressure, K-type thermocouple that was positioned within the main fluid cavity of the cell and was calibrated using ice and boiling water. Cell pressure was monitored by a pressure transducer that was calibrated against a NIST-traceable standard gauge. The transmission IR optics consisted of cylindrical ZnSe windows and a pathlength of ~4 cm. The internal reflection element (IRE) of the ATR IR optics was a single-reflection 45° prism made of Ge (Harrick Scientific). A detailed description of the fluid delivery apparatus, reaction cell, cell and manifold schematics, spectrometer settings, spectral collection procedures, titration loop calibrations, the general method for performing titrations, and data analysis procedures have been described in detail elsewhere (see https://doi.org/10.1063/1.4870411).[1] Modifications to the transmission IR pathlength and the method for water delivery have also been described previously (https://doi.org/10.1021/acs.jced.6b00999).[2]

For all experiments, transmission IR spectra were processed to remove spectral contributions due to baseline drift, water vapor in the spectrometer, and CO_2 from small variations (less than 0.4 bar) in pressure that occurred during the titrations. Each measured transmission IR spectrum was corrected by fitting the data to previously measured spectra of anhydrous $scCO_2$ and

water dissolved in $scCO_2$ at 50 °C and 90 bar. The wavenumber regions used in the least-squares analysis were 813–1107, 1228–1567, 1650–2044, and 3821–4250 cm^{-1}. These were chosen based on where dissolved water absorbs but is not too intense (i.e., off-scale) and where the bands of CO_2 do not significantly overlap. A linear baseline was also included in the fit for each wavenumber region. The residuals were almost exclusively the spectrum of water vapor within the spectrometer interferometer chamber due to fluctuations in the spectrometer's vacuum and the humidity of the purge gas. The integrated absorbances of the contribution from H_2O dissolved in the $scCO_2$ were calculated using the HOH bending mode region of dissolved water between 1650 and 2054 cm^{-1}.

ATR IR spectra were corrected for distortions[3, 4] by assuming a $scCO_2$ dominated system with a real refractive index of 1.065 (at wavelength of 632.8 nm),[5] converting to optical constant spectra using the method of Bertie et al.,[6, 7] and calculating absorbance spectra from these optical constants for a hypothetical 1 μm pathlength transmission cell using the Fresnel equations.[8, 9] After this ATR distortion correction, the spectrum of the Co-Doped forsterite exposed to anhydrous fluid was subtracted from each measured spectrum; thus, the background spectra in these analyses were those of the unreacted Co-Doped forsterite at pressure and temperature. Spectra were baseline corrected in the asymmetric CO stretching region by subtracting the line fit to absorbances from 1277 to 1281 cm^{-1} and 1760 to 1780 cm^{-1}.

X-Ray Diffraction (XRD). Powder XRD patterns were collected from powders packed into zero-background well holders using a Rigaku SmartLab SE diffractometer. The instrument employed Bragg-Brentano geometry with a Cu X-ray source (λ = 1.5418 Å), a variable divergence slit, and a high-speed D/teX Ultra 250 1D detector. Patterns were collected between 2 and 100 °2θ at intervals of 0.01 °2θ, scanning at 2°2θ/min. Quantitation of minerals was

performed by the Rietveld method using TOPAS (v6, Bruker AXS) and crystal structures from the Inorganic Crystal Structure Database (Fachinformationszentrum Karlsruhe, Germany). A weighed amount of corundum (Standard Reference Material 676a, NIST) was mixed into each sample to place the quantities on an absolute scale and allow the determination of amorphous/unidentified material by difference.

X-Ray Photoelectron Spectroscopy (XPS). XPS measurements were performed using a Thermo Fisher NEXSA spectrometer with a 125 mm mean radius, full 180° hemispherical analyzer, and 128-channel detector. This system uses a focused monochromatic Al Kα X-ray (1486.7 eV) source for excitation and an electron emission angle of 60 degrees. The narrow scan spectra were collected using a pass-energy of 50 eV with a step size of 0.1 eV. For the Ag $3d_{5/2}$ line, these conditions produced a FWHM of 0.84 eV ± 0.02 eV. The binding energy (BE) scale is calibrated using the Cu $2p_{3/2}$ feature at 932.62 ± 0.05 eV and Au $4f_{7/2}$ at 83.96 ± 0.05 eV.

Table S1. X-Ray Photoelectron Spectroscopy (XPS) Characterization of 25% Co-Doped Forsterite.[a]

	Co2p		Mg2p		Si2p		O1s			
Sample Position	**%**	**BE (eV)**	**%**	**BE (eV)**	**%**	**BE (eV)**	**%**	**BE (eV)**	**Co/(Co+Mg)**	**(Co+Mg)/Si**
1	6.6	782.3	16.8	51.2	13.5	102.9	63.2	531.8	0.28	1.7
2	6.3	782.2	16.8	51.2	13.4	102.9	63.6	531.7	0.27	1.7

[a] BE = binding energy, % = atomic percent. The uncertainty in the atomic percent is estimated to be 10%.

Table S2. Calibrations, Titrations, and Time-Dependent Experiments.

Experiments	**Techniques and Conditions**	**Purpose**
	<u>Calibrations</u>	
Cal_1; Cal_2	Transmission IR from in situ IR spectroscopic titrations in scCO_2 at 50 °C and 90 bar in the absence of Co-doped forsterite.	Correlate integrated absorbance of HOH bend to dissolved H_2O concentration; Determine concentration of H_2O required to saturate fluid.
	<u>Titrations</u>	
Ads_1; Ads_2	Transmission IR from in situ IR spectroscopic titrations in scCO_2 at 50 °C and 90 bar in the presence of Co-dope forsterite.	Correlate H_2O coverage to fluid RH.
	<u>Time-Dependent Experiments</u>	
TDep_1; TDep_2; TDep_3	ATR IR from in situ IR spectroscopic titrations in scCO_2 at 50°C and 90 bar in the presence of Co-doped forsterite, but as function of time after reaching target RH values of ~96%, ~85% or ~72%.	Quantify rates and extents of reaction as a function of time. Identify carbonation products.

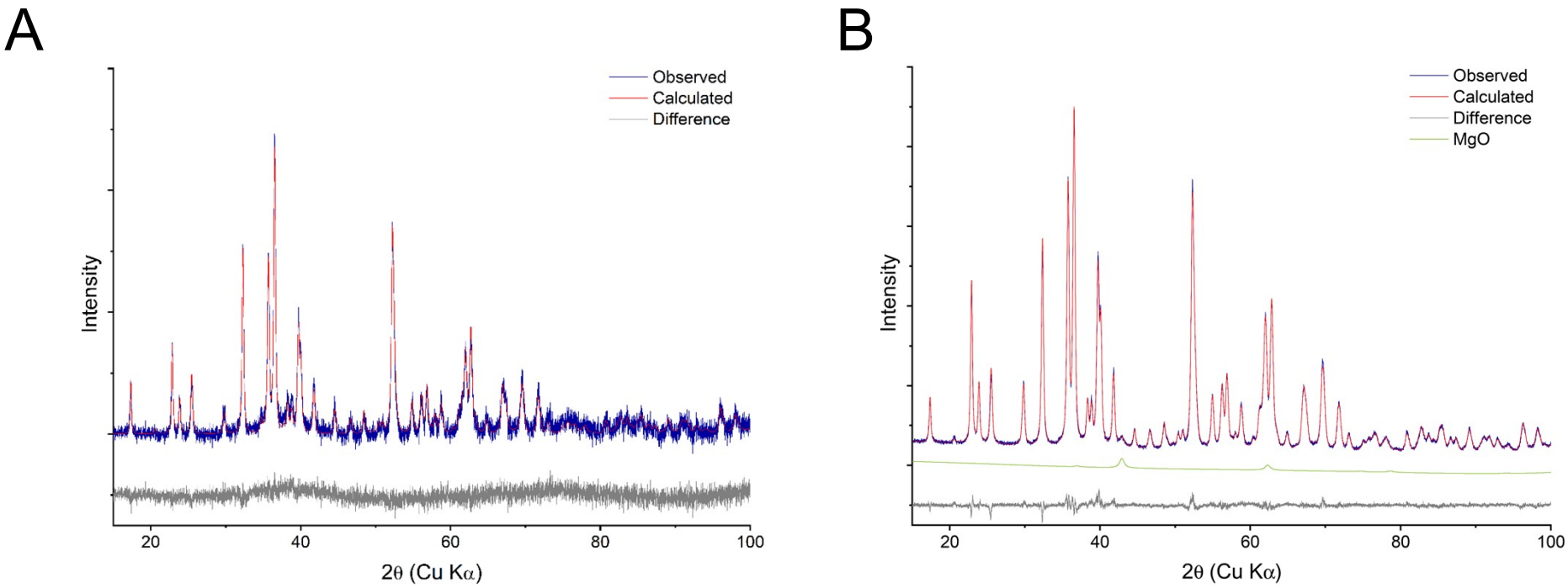

Figure S1. (A) XRD pattern of Co-doped forsterite with a Rietveld fit based on the forsterite structure published by Hushur et al.[10] The measured pattern has been background corrected to account for Co fluorescence. The absorption and fluorescence of X-rays from Co reduce the elastic scattering intensity and increase noise. Although the lower elastic scattering intensity degrades the signal-to-noise ratio, we are still able to fit the Co content with sufficient precision. Refinement of Co substitution on the Mg sites indicated that Co occupancy was 0.330(5) in the M1 site and 0.102(5) in the M2 site. The overall refined Co content was therefore 0.22(1), which is close to the expected 0.25. The crystal parameters were a=4.758(1) Å, b=10.218(1) Å, c=5.980(1) Å. The strain e_0 was 0.00008, and the crystallite size was 37 nm. The weighted profile R-factor (R_{wp}) for the fit was 1.27%. (B) Rietveld fit of undoped forsterite based on the same structure, containing 1.5% MgO (contribution shown in green). The refined lattice parameters were a=4.753(1) Å, b=10.197(1) Å, c=5.980(1) Å. The strain e_0 was 0.00051, and the crystallite size was 30 nm. The weighted profile R-factor (R_{wp}) for the fit was 4.26%.

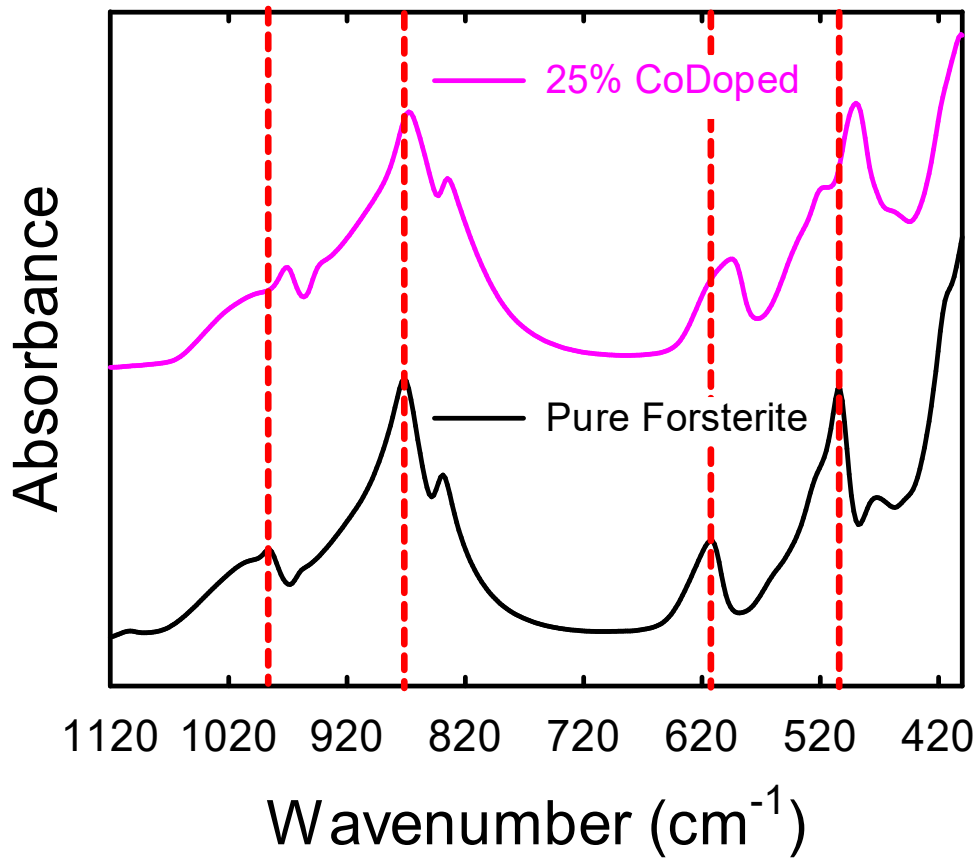

Figure S2. Infrared spectrum of Co-doped forsterite (top, magenta) compared to that of pure forsterite (bottom, black). Vertical dashed red lines are to facilitate the visualization of differences in peak positions.

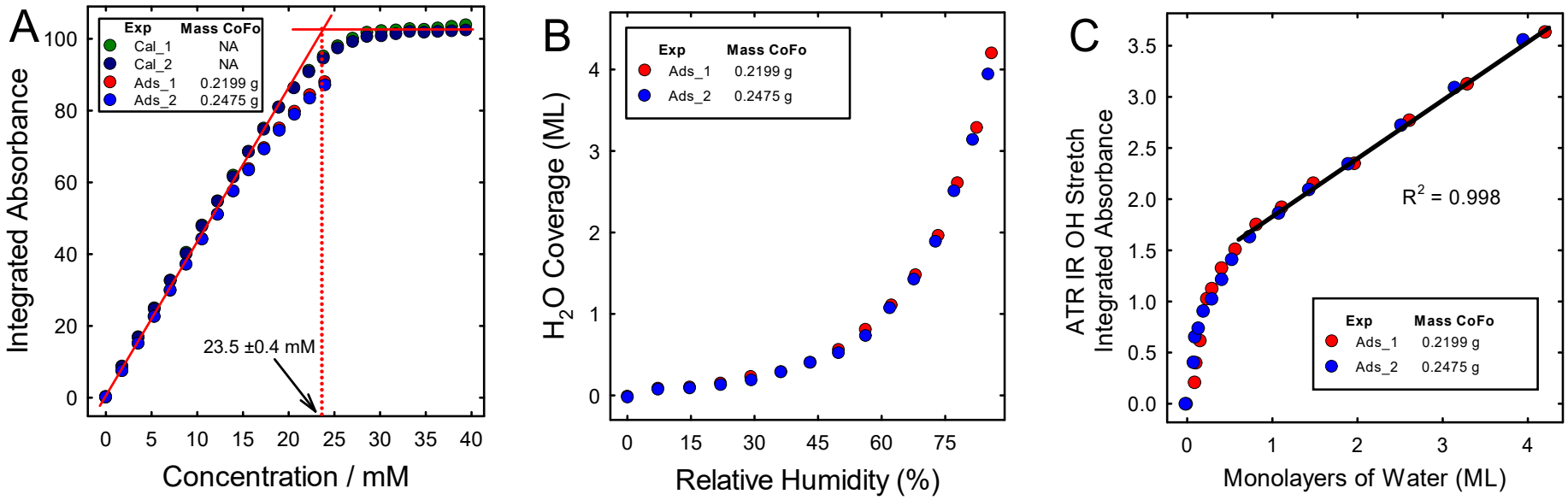

Figure S3. (A) Integrated absorbance of the HOH bending mode of dissolved H_2O versus total H_2O concentration for calibration experiments (indicated by "Cal" in the experiment name; see Table S2) and adsorption experiments (indicated by "Ads" in the experiment name; see Table S2). For the calibration experiments, the intersection of the line fits through the linear and plateau regions of the data is the dissolved H_2O concentration at saturation. (B) Average water film thickness as a function of relative humidity (RH) for experiments Ads_1 and Ads_2. (C) The integrated absorbance in the OH stretching region (specifically, between 3021 and 3533 cm^{-1}) as a function of water film thickness. The black line is the linear least squares fit to the data beyond 1 monolayer of water. This correlation was used to estimate the average water film thickness in experiments TDep_1 through TDep_3.

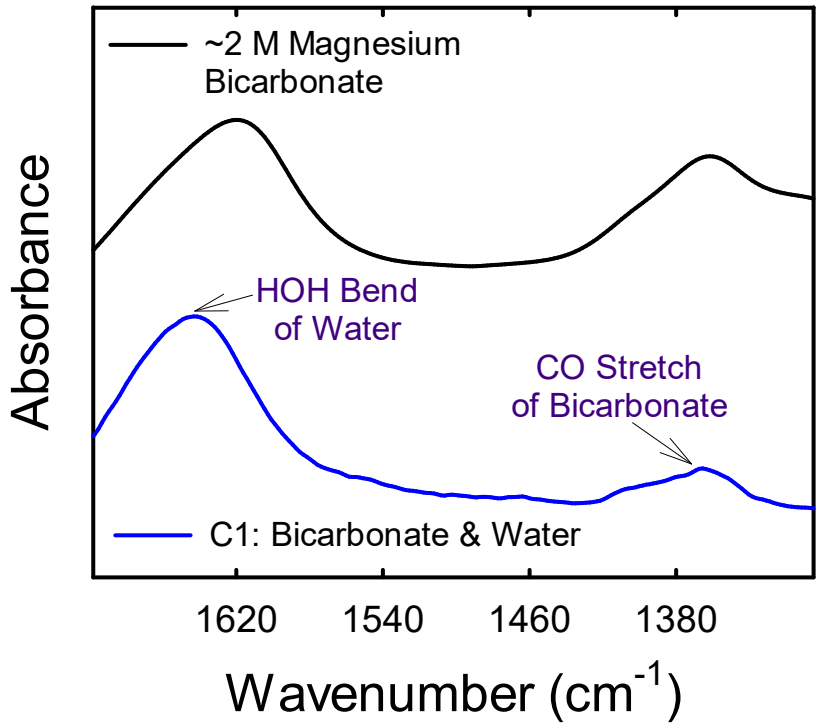

Figure S4. (Top, black) The IR spectrum of ~2 M aqueous magnesium bicarbonate. (Bottom, blue) Component C1 from the two-component MCR-ALS analysis of the combined spectra from TDep_1 at 96% RH, TDep_2 at 85% RH, and TDep_3 at 72% RH.

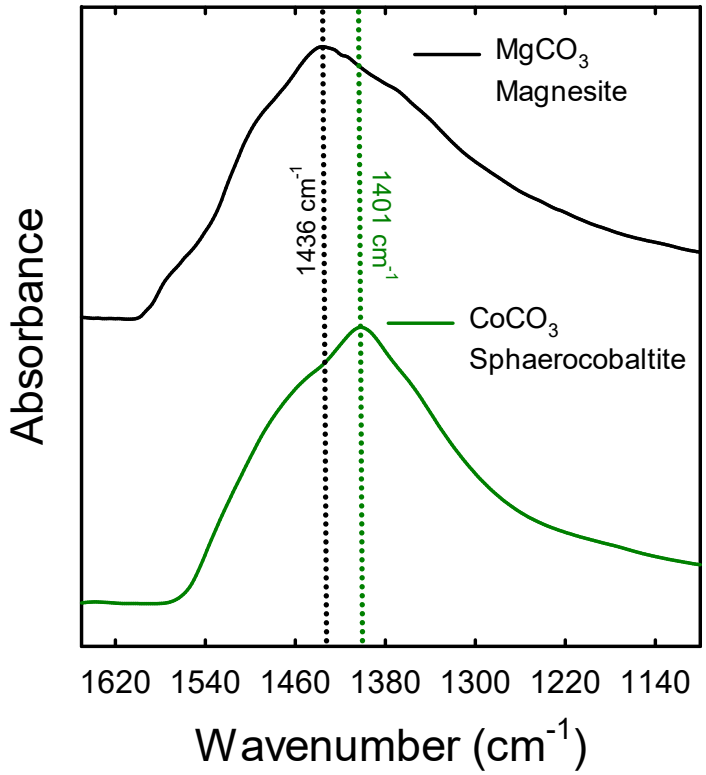

Figure S5. IR spectra in the CO stretching band region of $MgCO_3$ (magnesite) synthesized in Qafoku et al.[11] (Top, black) and of $CoCO_3$ (sphaerocobaltite) synthesized in Riechers et al.[12] (Bottom, green).

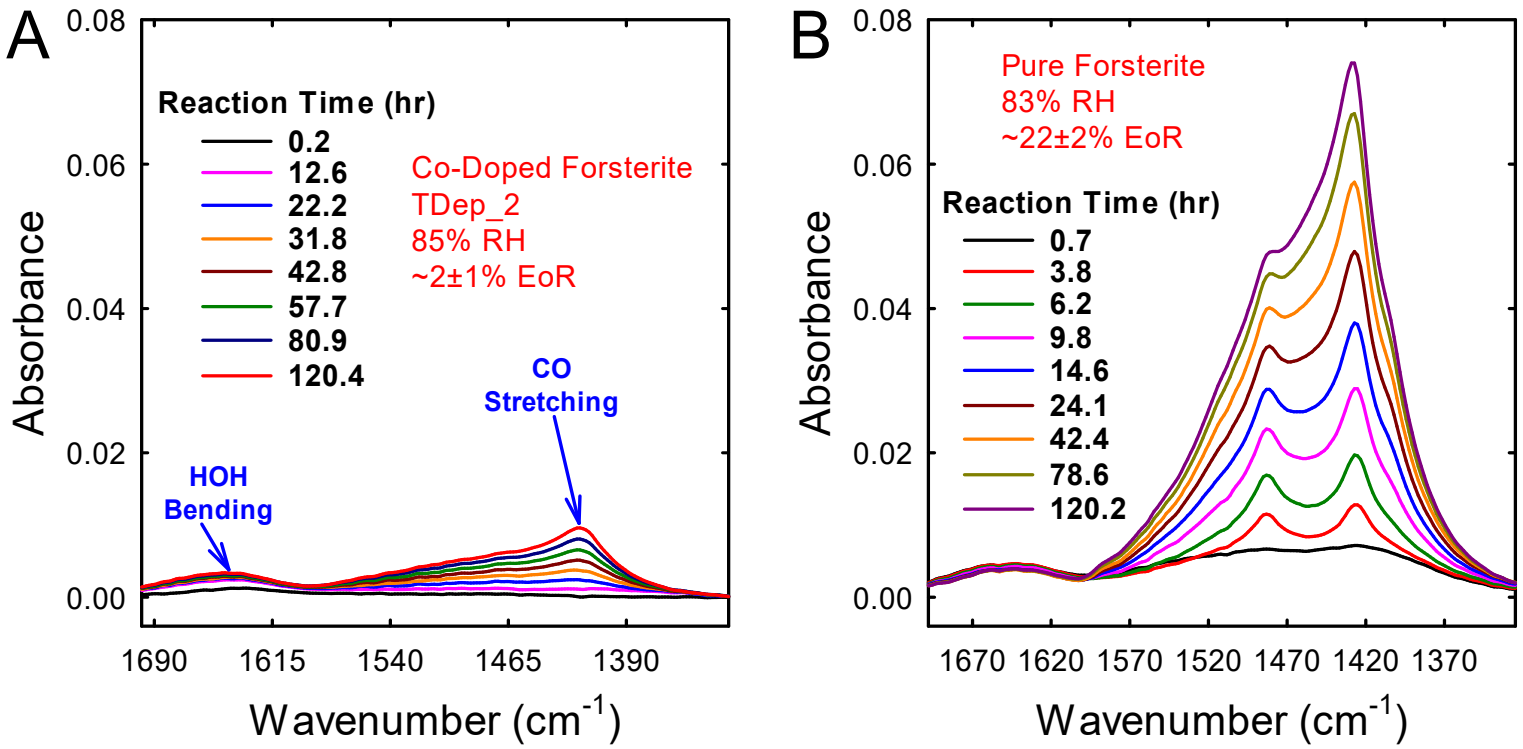

Figure S6. Select ATR IR spectra from (A) experiment TDep_2 at 85% RH and (B) a previously reported[13] experiment with pure forsterite at 83% RH (50 °C and 90 bar). Spectral absorbances have been normalized for the surface area of the pure forsterite (42.3 m^2/g) versus the Co-doped forsterite (20.1 m^2/g). The background spectra were the unreacted minerals at pressure and temperature. Pure forsterite carbonates first to amorphous magnesium carbonate that is replaced by predominantly hydromagnesite after ~6 hrs, at which point magnesite growth takes over for the remainder of the experiment. Co-doped forsterite carbonates to Co-doped magnesite (see Figures 3 and S5), and we do not detect any intermediate carbonate phases.

References

1. C. J. Thompson, P. F. Martin, J. Chen, P. Benezeth, H. T. Schaef, K. M. Rosso, A. R. Felmy and J. S. Loring, *Rev Sci Instrum*, 2014, **85**.
2. J. S. Loring, D. H. Bacon, R. D. Springer, A. Anderko, S. Gopinath, C. M. Yonkofski, C. J. Thompson, B. P. McGrail, K. M. Rosso and H. T. Schaef, *Journal of Chemical & Engineering Data*, 2017, **62**, 1608-1614.
3. M. Boulet-Audet, T. Buffeteau, S. Boudreault, N. Daugey and M. Pézolet, *The Journal of Physical Chemistry B*, 2010, **114**, 8255-8261.
4. N. J. Harrick, *Internal Reflection Spectroscopy*, John Wiley & Sons, New York, 1967.
5. G. J. Besserer and D. B. Robinson, *Journal of Chemical & Engineering Data*, 1973, **18**, 137-140.
6. J. E. Bertie and H. H. Eysel, *Applied Spectroscopy*, 1985, **39**, 392-401.
7. J. E. Bertie, S. L. Zhang and R. Manji, *Applied Spectroscopy*, 1992, **46**, 1660-1665.
8. K. Ohta and H. Ishida, *Appl. Opt.*, 1990, **29**, 1952-1959.
9. J. S. Loring and D. P. Land, *Appl. Opt.*, 1998, **37**, 3515-3526.
10. A. Hushur, M. H. Manghnani, J. R. Smyth, F. Nestola and D. J. Frost, *American Mineralogist*, 2009, **94**, 751-760.
11. O. Qafoku, D. A. Dixon, K. M. Rosso, H. T. Schaef, M. E. Bowden, B. W. Arey and A. R. Felmy, *Environmental Science & Technology*, 2015, **49**, 10736-10744.
12. S. L. Riechers, E. S. Ilton, O. Qafoku, Y. Du and S. N. Kerisit, *Chemical Geology*, 2022, **605**, 120951.
13. S. T. Mergelsberg, B. P. Rajan, B. A. Legg, L. Kovarik, S. D. Burton, G. M. Bowers, M. E. Bowden, O. Qafoku, C. J. Thompson, S. N. Kerisit*, et al.*, *Environmental Science & Technology Letters*, 2023, **10**, 98-104.